J. Fluid Mech. (2008), *vol.* 596, *pp.* 387–412.
DOI: 10.1017/S0022112007009603 Printed in the United Kingdom

Sound transmission in strongly curved slowly varying cylindrical ducts with flow

By E. J. BRAMBLEY AND N. PEAKE

Department of Applied Mathematics and Theoretical Physics, University of Cambridge, Centre for Mathematical Sciences, Wilberforce Road, Cambridge CB3 0WA, United Kingdom

(Received 1 May 2007 and in revised form 3 September 2007)

In this paper we consider the propagation of acoustic waves on top of an inviscid steady flow along a curved hollow or annular duct with hard or lined walls. The curvature of the duct centreline (which is not restricted to being small) and the wall radii vary slowly along the duct, allowing application of an asymptotic multiple scales analysis. The modal wavenumbers and mode shapes are determined locally as modes of a torus with the same local curvature, while the amplitude of the modes evolves as the mode propagates along the duct. The duct modes are found explicitly at each axial location using a pseudospectral numerical method.

Unlike the case of a straight duct carrying uniform flow, there is a fundamental asymmetry between upstream and downstream propagating modes, with some mode shapes tending to be concentrated on either the inside or outside of the bend depending on the direction of propagation, curvature and steady-flow Mach number. The interaction between the presence of wall lining and curvature is also significant; for instance, in a representative case it is found that the curvature causes the first few acoustic modes to be more heavily damped by the duct boundary than would be expected for a straight duct.

Using ray theory, we suggest explanations of these features. For the lowest azimuthal-order modes, three distinct regimes are found in which the modes are localized in different parts of the duct cross-section. This phenomenon is explained by a balance between whispering-gallery effects along the duct and refraction by the steady flow. At the opposite extreme, strongly spinning modes are investigated, and are seen to be due to a different whispering-gallery effect across the duct cross-section.

1. Introduction

The propagation of acoustic waves along curved pipes has attracted much attention, with a wide range of applications. One application, which is the motivation for the research described in the current paper, is the prediction of unsteady flow along the sort of convoluted intakes often found on the engines of military aircraft. One issue here might be the behaviour of sound generated by the fan as it propagates upstream, or alternatively (but not within the scope of this paper) at very large amplitudes the propagation of surge events.

A selection of previous work will be mentioned here. Keefe & Benade (1983) used ideas of impedance matching to study the propagation of very long waves along a curved pipe. Pagneux and coworkers have developed multimodal techniques to describe propagation in various sorts of curved ducts with zero mean flow (Pagneux, Amir & Kergomard 1996*a*,*b*; Felix & Pagneux 2001, 2002). Felix & Pagneux (2004) have also studied sound

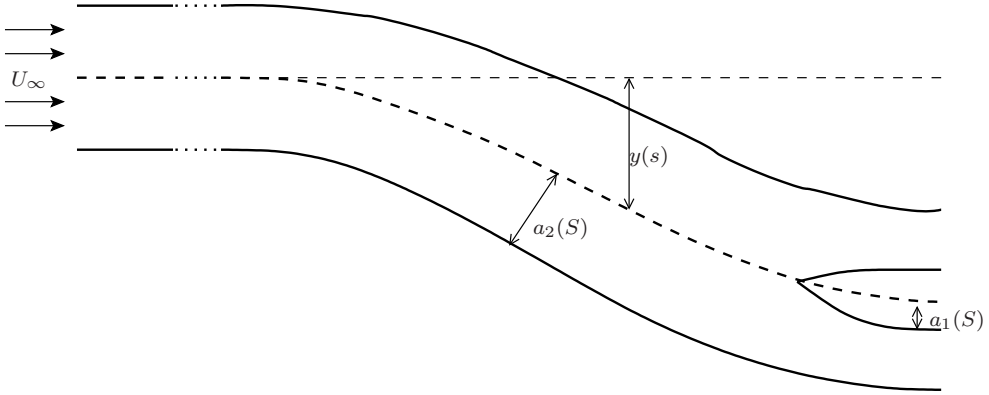

FIGURE 1. Schematic of the duct geometry.

attenuation round a lined bend, including a ray-tracing explanation of the effects of curvature, although this was still for zero mean flow. More analytically based studies have tended to use specific limits, including slender curved ducts (Ting & Miksis 1983) and weakly curved ducts in two and three dimensions (Gridin & Craster 2003; Adamou, Gridin & Craster 2005).

In a different direction, including mean flow for a straight duct with a circular cross-section that varies slowly in the axial direction, Rienstra (1999) derived a multiple-scales approximation for the unsteady field. This approximation has been validated by Rienstra & Eversman (2001) by comparison with finite-element computations. Rienstra's analysis has been extended in a number of ways; by Rienstra (2003*b*) to the case of arbitrary duct cross-section, by Cooper & Peake (2001) to the case of swirling mean flow, and by Ovenden (2005) to a uniformly valid solution that allows modes to undergo cuton–cutoff transition. However, all of this has been for straight ducts. The aim of this paper is therefore to investigate both curvature and mean flow simultaneously.

The paper is organised as follows. In §2 we derive the steady potential mean flow through a curved duct. The unsteady linearized flow is described in §3; as a mode propagates along the duct it is distorted, and the description of this process involves first the determination of the local axial wavenumber and mode shape, and second the determination of the slowly varying amplitude. This local eigenvalue problem must be solved numerically, and our pseudospectral method for doing this is described in §4. Results are presented in §5, and the possibility of a mode transitioning from cuton to cutoff is investigated in §6. Finally, in §7, ray-tracing theory is used to shed some light on the structure of the duct modes, and to investigate the intriguing localization phenomenon discovered in previous sections.

2. Steady mean flow

We consider a duct, as shown in figure 1, whose centreline possesses nonzero curvature but zero torsion (i.e. the centreline lies in a plane). The duct has a circular cross-section in planes normal to the centreline, and can be either hollow or annular. We pick out two lengthscales for such a duct. The first, ℓ^* (* denotes dimensional variables), is the lengthscale associated with the geometry of the duct at a given axial location, so that the duct radius $a^*_{1,2}$ is of order ℓ^* and the duct curvature κ^* is of order $1/\ell^*$. This means the radius of curvature is on the same scale as the duct radius; were these two of different scales some asymptotic simplification becomes possible, but here we deal with the full

generality. The cases of a slender curved duct or a straight duct of varying radius then follow as special cases. The second lengthscale, L^*, is the shortest lengthscale along the duct centreline over which these parameters vary.

Let us now be more specific. Let s^* be the arc-length along the duct centreline. Far upstream ($s^* \to -\infty$) the duct is assumed to be straight and of uniform outer radius ℓ^*. (Throughout this paper, the term *straight* refers to a duct with a straight centreline (zero curvature), irrespective of variations of the inner and outer radii.) The radii of the inner (and outer) walls and the centreline curvature then vary along the duct on the lengthscale L^*, so that the inner and outer radii $a^*_{1,2}$ and the centreline curvature κ^* are functions of $S \equiv s^*/L^*$. The requirement of slow variation along the axis is then equivalent to $\epsilon \equiv l^*/L^* \ll 1$. The duct carries a mean flow, which far upstream has uniform density D^*_∞, speed U^*_∞ and sound speed C^*_∞. In what follows speeds are non-dimensionalized by C^*_∞, densities by D^*_∞, distances by ℓ^*, times by ℓ^*/C^*_∞, and pressures by $(C^*_\infty)^2 D^*_\infty$. We introduce the duct-centred coordinate system (s, r, θ), where r, θ are polar coordinates in planes normal to the duct centreline, and s is the arc-length along the centreline. The duct inner and outer radii are $a_{1,2}(S)$ and the centreline curvature is $\kappa(S)$, where $S = \varepsilon s$ is the nondimensionalized slow coordinate over which the duct geometry varies.

The steady velocity in the duct is written $\boldsymbol{U} = U\boldsymbol{e_s} + V\boldsymbol{e_r} + W\boldsymbol{e_\theta}$, and it is assumed that all steady-mean-flow variables are functions of r, θ, S, i.e. vary slowly down the duct. The geometric factor associated with the curvilinear coordinate s is $h_s = 1 - \kappa(S) r \cos\theta$. We assume an inviscid irrotational perfect gas with ratio of specific heats γ. We apply the steady continuity condition $\boldsymbol{\nabla} \cdot (D\boldsymbol{U}) = 0$,

$$\frac{\varepsilon}{h_s}\frac{\partial}{\partial S}(DU) + \frac{1}{r h_s}\frac{\partial}{\partial r}(r h_s DV) + \frac{1}{r h_s}\frac{\partial}{\partial \theta}(h_s DW) = 0,$$

together with the condition for irrotational mean flow, $\boldsymbol{\nabla} \wedge \boldsymbol{U} = 0$,

$$\frac{1}{r}\frac{\partial}{\partial r}(rW) - \frac{1}{r}\frac{\partial V}{\partial \theta} = 0, \quad \frac{1}{r h_s}\frac{\partial}{\partial \theta}(h_s U) - \frac{\varepsilon}{h_s}\frac{\partial W}{\partial S} = 0, \quad \frac{\varepsilon}{h_s}\frac{\partial V}{\partial S} - \frac{1}{h_s}\frac{\partial}{\partial r}(h_s U) = 0,$$

and the irrotational form of Bernoulli's equation,

$$\frac{1}{2}U^2 + \frac{1}{\gamma - 1}D^{\gamma - 1} = H, \tag{2.1}$$

where the enthalpy $H = {U_\infty}^2/2 + 1/(\gamma - 1)$ is a constant determined at upstream infinity. For the steady flow, the duct walls are considered perfectly hard and impenetrable, with the corresponding boundary conditions

$$V - \frac{\varepsilon}{h_s}\frac{\mathrm{d}a_j}{\mathrm{d}S}U = 0 \qquad \text{at } r = a_j(S) \quad j = 1, 2\,. \tag{2.2}$$

We assume no leading-order potential swirl, so that W vanishes to leading order. Putting all these assumptions together, we find that

$$D = D_0 + O(\varepsilon^2), \quad U = U_0 + O(\varepsilon^2), \quad V = \varepsilon V_1 + O(\varepsilon^3), \quad W = \varepsilon W_1 + O(\varepsilon^3),$$

where

$$U_0(S, r, \theta) = \frac{U_\dagger(S)}{h_s(r, \theta, S)}, \qquad D_0 = \left[(\gamma - 1)\left(H - \frac{1}{2}{U_0}^2\right)\right]^{1/\gamma - 1}.$$

The quantity $U_\dagger$ may be found in terms of U_∞ by applying conservation of mass at

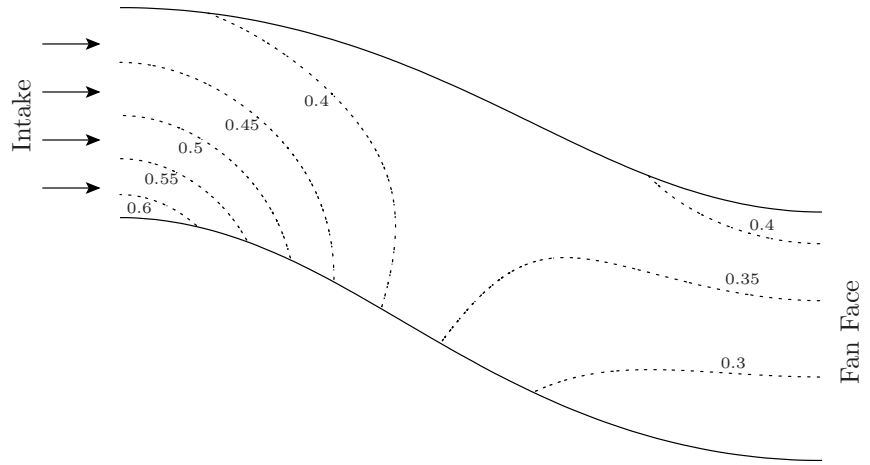

FIGURE 2. Contours of the axial mean flow Mach number in the RAE 2129 Inlet Diffuser. Far upstream is a uniform-inlet Mach number of 0.5.

different axial locations, to yield the implicit equation

$$\int_0^{2\pi}\int_{a_1}^{a_2} U_0 D_0 r \,\mathrm{d}r\,\mathrm{d}\theta = \pi U_\infty \big(1 - a_1(-\infty)\big)^2, \tag{2.3}$$

which can easily be solved numerically. Note that the mean velocity components in the plane of cross-section arise, in irrotational flow, from the slow variation of the duct, and are therefore $O(\epsilon)$. In what follows it turns out that the value of the radial velocity V_1 is only required on the walls, and can be found simply from the $O(\epsilon)$ terms in the boundary condition (2.2). The value of the $O(\varepsilon)$ tangential velocity W_1 will not be required at all in our final answer for the unsteady flow.

One duct geometry we shall consider in particular is the RAE 2129 Inlet Diffuser duct (as considered by Menzies 2002), which is a much studied reference duct geometry. A cross-section along the RAE 2129 duct centreline is shown in figure 2, along with the mean flow for a uniform-inlet Mach number $U_\infty = 0.5$. The duct geometry is defined in terms of the lateral offset of the centreline, y^*, from its position at the intake $s^* = 0$ (as shown in figure 1), with

$$y^*(s^*) = -\frac{h^*}{2}\left(1 - \cos\left(\frac{\pi s^*}{L^*}\right)\right) , \tag{2.4}$$

The lateral offset at the downstream exit ($s^* = L^*$) is then $-h^*$. The duct itself is hollow, with outer radius varying quartically between upstream (radius ℓ^*) and downstream (radius a_f^*) as

$$\frac{a^*(s^*) - \ell^*}{a_f^* - \ell^*} = 3\left(1 - \frac{s^*}{L^*}\right)^4 - 4\left(1 - \frac{s^*}{L^*}\right)^3 + 1 .$$

For the RAE 2129 duct, $L^*/\ell^* = 7.1$, $h^*/L^* = 0.3$ and $(a_f^*/\ell^*)^2 = 1.4$. This leads to a value of ε based on the duct length of $\varepsilon = 1/7.1$, for which it is reasonable to suppose that the small-ε asymptotics of this paper will work well.

3. Unsteady flow

Consider a small time-dependent perturbation $(\boldsymbol{u}, \rho, p)$ with time dependence $\exp\{\mathrm{i}\omega t\}$ to the mean flow $(\boldsymbol{U}, D, P)$. Introducing a scalar potential $\boldsymbol{u} = \boldsymbol{\nabla}\phi$, and neglecting vortical and entropic perturbations, the equations for the unsteady linearized flow due to Goldstein (1978) reduce to

$$\frac{\mathrm{D}}{\mathrm{D}t}\left(\frac{1}{C^2}\frac{\mathrm{D}\phi}{\mathrm{D}t}\right) - \frac{1}{D}\boldsymbol{\nabla}\cdot\left(D\boldsymbol{\nabla}\phi\right) = 0, \qquad p = C^2\rho = -D\frac{\mathrm{D}\phi}{\mathrm{D}t}, \tag{3.1}$$

where $\mathrm{D}/\mathrm{D}t = \mathrm{i}\omega + \boldsymbol{U}\cdot\boldsymbol{\nabla}$ is the convective derivative with respect to the mean flow, and $C^2 = D^{\gamma-1}$ is the square of the wave speed. (A similar, although less general, equation describing sound propagation through a nonuniform medium was originally given by Blokhintzev 1946.) Equation (3.1) is to be solved subject to the usual Myers (1980) boundary condition for a lined duct, namely

$$\mathrm{i}\omega\boldsymbol{n}\cdot\boldsymbol{\nabla}\phi = \Big\{\mathrm{i}\omega + \boldsymbol{U}\cdot\boldsymbol{\nabla} - \big[(\boldsymbol{n}\cdot\boldsymbol{\nabla})\boldsymbol{U}\big]\cdot\boldsymbol{n}\Big\}(p/Z_j) \qquad \text{on } r = a_j(S) \text{ for } j = 1, 2\,, \tag{3.2}$$

where $Z_{1,2}(S)$ are the wall impedances and $\boldsymbol{n}$ is the corresponding wall normal pointing out of the fluid. (Note that, had an $\exp\{-\mathrm{i}\omega t\}$ convention been adopted, $Z_{1,2}$ would be the complex conjugate of what it is here.)

In order to account for the slowly varying duct geometry and mean flow we follow Rienstra (1999) and pose the multiple-scales WKB ansatz (see for instance Hinch 1991, chapter 7)

$$\phi = \big[A_0(S, r, \theta) + \varepsilon A_1(S, r, \theta) + O(\varepsilon^2)\big]\exp\left\{\mathrm{i}\omega t - \frac{\mathrm{i}}{\varepsilon}\int_0^S k(S')\,\mathrm{d}S'\right\}\,.$$

The details of what follows are given in appendix A. In short, substituting this into (3.1) and taking just the $O(1)$ terms gives

$$\frac{1}{h_s D_0}\left[\frac{1}{r}\frac{\partial}{\partial r}\left(r h_s D_0 \frac{\partial A_0}{\partial r}\right) + \frac{1}{r^2}\frac{\partial}{\partial\theta}\left(h_s D_0 \frac{\partial A_0}{\partial\theta}\right)\right] + \left(\frac{\Lambda^2}{{C_0}^2} - \frac{k^2}{{h_s}^2}\right)A_0 = 0\,, \tag{3.3}$$

where $\Lambda = \omega - kU_0/h_s$ and ${C_0}^2 = {D_0}^{\gamma-1}$. The $O(1)$ boundary condition from (3.2) is

$$\frac{\partial A_0}{\partial r} = \pm\frac{D_0\Lambda^2 A_0}{\mathrm{i}\omega Z_j} \qquad \text{on } r = a_j(S) \text{ for } j = 1, 2\,, \tag{3.4}$$

where $\pm$ refers to the outer and the inner walls respectively. For hard walls (3.4) becomes simply $\partial A_0/\partial r = 0$. One crucial difference here from the case of a straight circular duct is the highly nontrivial dependence of A_0 on θ. When $\kappa = 0$, (3.3) and (3.4) can be solved using separation of variables to yield a well-known solution proportional to $\exp\{-\mathrm{i}m\theta\}$ for integer m and depending on Bessel functions in the radial direction. But when $\kappa \neq 0$, (3.3) is no longer separable. Equations (3.3) and (3.4) must therefore be solved numerically to determine the axial wavenumber $k(S)$ and the corresponding wave function $A_0(S, r, \theta)$. Details are given in the next section. For definiteness, we normalize the solution so that

$$A_0(S, r, \theta) = N(S)\hat{A}_0(S, r, \theta), \qquad \int_0^{2\pi}\int_{a_1}^{a_2}\frac{D_0 U_0\omega}{{C_0}^2}{\hat{A}_0}^2\, r\,\mathrm{d}r\,\mathrm{d}\theta = 1. \tag{3.5}$$

The reason for this strange-looking normalization is that it becomes much more natural when we consider turning point in §6. The unknown amplitude $N(S)$ must be determined from the solvability condition obtained using the $O(\varepsilon)$ terms from (3.1) and (3.2), following the procedure given by Rienstra (1999). The details of this are given in appendix A.

In short, by multiplying the $O(\varepsilon)$ part of (3.1) by $h_s D_0 A_0$, integrating across the duct cross section, and applying the mean flow equations of motion to eliminate V_1 and W_1, we arrive at the requirement that the quantity

$$\left\{F(S) + I_1(S) + I_2(S)\right\} N(S)^2 \tag{3.6}$$

is independent of S, where

$$F(S) = \int_0^{2\pi}\int_{a_1}^{a_2} D_0 {\hat{A}_0}^2 \left[\frac{\omega U_0}{{C_0}^2} + \frac{k}{h_s}\left(1 - \frac{{U_0}^2}{{C_0}^2}\right)\right] r \,\mathrm{d}r \,\mathrm{d}\theta \,,$$
$$I_j(S) = \left[\int_0^{2\pi} \frac{\Lambda U_0 {D_0}^2 r}{\mathrm{i}\omega Z_j} {\hat{A}_0}^2 \mathrm{d}\theta\right]_{r=a_j} .$$

Notice here that this condition involves ${\hat{A}_0}^2$, rather than $|\hat{A}_0|^2$, which has arisen from the non-self-adjoint nature of the k eigenvalue problem (in fact the adjoint solution is A_0^*). In the case of rigid walls (3.6) reduces to the condition that $F(S)N(S)^2$ is constant along the duct, which for cuton modes can be interpreted as conservation of energy. For finite impedance, acoustic energy from the flow is dissipated by the walls, and this effect manifests itself in both the fact that the axial eigenvalue $k(S)$ will be complex and by the presence of the surface integrals $I_{1,2}(S)$ in (3.6). Note that $I_{1,2}$ are both additive in (3.6), corresponding to the fact that energy is dissipated at both walls.

Putting all this together, we now have the leading-order solution (3.5) for the unsteady flow, in which the local axial wavenumber and mode shape are determined by numerical solution of (3.3) and (3.4) and the slowly varying amplitude is then given by (3.6).

4. Numerical solution

Our task is to solve the leading-order eigenvalue problem (3.3) and (3.4) so as to determine the local axial wavenumber k and corresponding eigenfunctions as functions of the slow arc length S. The leading-order equation for A_0 and k is recast, by introducing $B_0 = kA_0$, as the generalised eigenvalue problem

$$\begin{pmatrix} \mathcal{L} & 0 \\ 0 & 1 \end{pmatrix} \begin{pmatrix} A_0 \\ B_0 \end{pmatrix} = k \begin{pmatrix} \dfrac{2\omega U_0}{h_s {C_0}^2} & \dfrac{1}{{h_s}^2}\left(1 - \dfrac{{U_0}^2}{{C_0}^2}\right) \\ 1 & 0 \end{pmatrix} \begin{pmatrix} A_0 \\ B_0 \end{pmatrix}, \tag{4.1}$$

where

$$\mathcal{L}A_0 = \frac{1}{h_s D_0}\left[\frac{1}{r}\frac{\partial}{\partial r}\left(r h_s D_0 \frac{\partial A_0}{\partial r}\right) + \frac{1}{r^2}\frac{\partial}{\partial \theta}\left(h_s D_0 \frac{\partial A_0}{\partial \theta}\right)\right] + \frac{\omega^2}{{C_0}^2} A_0,$$

subject to the boundary conditions

$$\pm\frac{\partial A_0}{\partial r} + \frac{\mathrm{i}\omega D_0}{Z_{1,2}} A_0 = k\left(\frac{2\mathrm{i}U_0 D_0}{h_s Z_{1,2}} A_0 - \frac{\mathrm{i}D_0 {U_0}^2}{{h_s}^2 \omega Z_{1,2}} B_0\right),$$

where the negative sign is taken for the inner boundary (if one is present), and the positive sign for the outer boundary.

We use a pseudospectral method with Chebyshev polynomials as the radial basis (see for example Khorrami, Malik & Ash 1989; Boyd 2001, chapter 18.6, p. 391) and trigonometric polynomials in the azimuthal direction. The number of collocation points in the radial and azimuthal directions are denoted by n_r and n_θ respectively (note that n_θ must be odd, since all trigonometric polynomials have an odd number of degrees of freedom).

For an annular duct, the collocation points are given by

$$(r_j, \theta_\ell) = \left(\frac{a_1 + a_2}{2} + \frac{a_1 - a_2}{2} \cos\left(\frac{j\pi}{n_r - 1} \right), \frac{2\ell\pi}{n_\theta} \right), \qquad \begin{cases} j = 0, \ldots, n_r - 1, \\ \ell = 0, \ldots, n_\theta - 1. \end{cases}$$

For a hollow duct, a_1 is replaced by a small nonzero constant, typically of the order of the spacing between neighbouring collocation points at the centre, $a_1 \approx a_2\pi^2/(2n_r - 2)^2$. While this is ugly, it allows both annular and hollow cases to be calculated using the same numerical code, and offers the potential to treat a hollow-to-annular transition (as pointed out by Rienstra 1999). For alternative ways to discretize a hollow duct, see Boyd (2001, chapter 18.5, pp. 386–391).

Our system is now discretized for an annular duct by requiring the boundary conditions to be satisfied at collocation points $(0, \ell)$ and $(n_r - 1, \ell)$ for $\ell = 0, \ldots, n_\theta - 1$, and (4.1) to be satisfied at collocation points (j, ℓ) for $\ell = 0, \ldots, n_\theta - 1$ and $j = 1, \ldots, n_r - 2$. For a hollow duct, (4.1) is also required to be satisfied at collocation points $(0, \ell)$ for $\ell = 0, \ldots, n_\theta - 1$, and the inner boundary condition is dropped. After a series of manipulations, which include representation of the r and θ derivatives using standard spectral differentiation matrices, we arrive at a generalised eigenvalue problem which is $2n_\theta n_r$ square. This was solved using the QZ algorithm, as implemented in the LAPACK library routine `ZGGEV` (Anderson *et al.* 1999).

In order to avoid spurious eigenvalues, two filtering processes were used. In the first, based loosely on the description by Boyd (2001, pp. 137–139), eigenvalues which vary significantly with small changes in the discretization are discarded. Second, we discard eigenvectors for which n_r or n_θ are not large enough to resolve properly the true eigenfunction. This is done by decomposing the numerical eigenvector into its spectral representation in both r and θ directions, and then ensuring that the outlying spectral coefficients are sufficiently small. Typically two thirds of the eigenvalues computed failed these tests, although this fraction is strongly dependent on the parameters used.

We validated our numerical calculations by comparison with known analytic results for the straight hard-walled ducts, and with numerical results for a lined straight pipe. An exponential decrease in error with increasing (n_r, n_θ) is obtained, as is expected from a pseudospectral method. The results presented in the next section were computed using typically $n_r \times n_\theta = 31 \times 61$. For hollow ducts, a value of $a_1 = 10^{-3}a_2$ was found to give good convergence.

5. Results

We first consider a hypothetical duct, with upstream conditions $U_\infty = 0.5$, $a_1 = 0.4$, $a_2 = 1.0$, $\gamma = 1.4$ and $\omega = 10$. The curvature of the duct was considered to vary slowly from $\kappa = 0$ upstream to $\kappa = 0.1$, at which point the spectrum is calculated. The numerical eigenvalues for this duct with hard walls are shown in figures 3(*a,b*). Figures 3(*c,d*) show examples of cross-sectional modal shapes. Both of these are upstream propagating modes, and the fundamental mode (the curved-duct equivalent of a plane-wave mode) in figure 3(*c*) is seen to be localized in the inside of the bend. The downstream propagating modes have similar shapes, but are localized on the outside of the bend. Figures 3(*e,f*) show typical higher-order modes, both of which are cutoff. These modal shapes are termed *bouncing-ball* and *whispering-gallery* type modes respectively, see Babic & Buldyrev (1991).

One interesting feature of the spectrum is the diagonal vanes of eigenvalues occurring periodically across the usual vertical line of cutoff modes in figure 3(*a*) and in close-up in figure 3(*b*). This feature only seems to appear in the presence of both non-zero mean flow

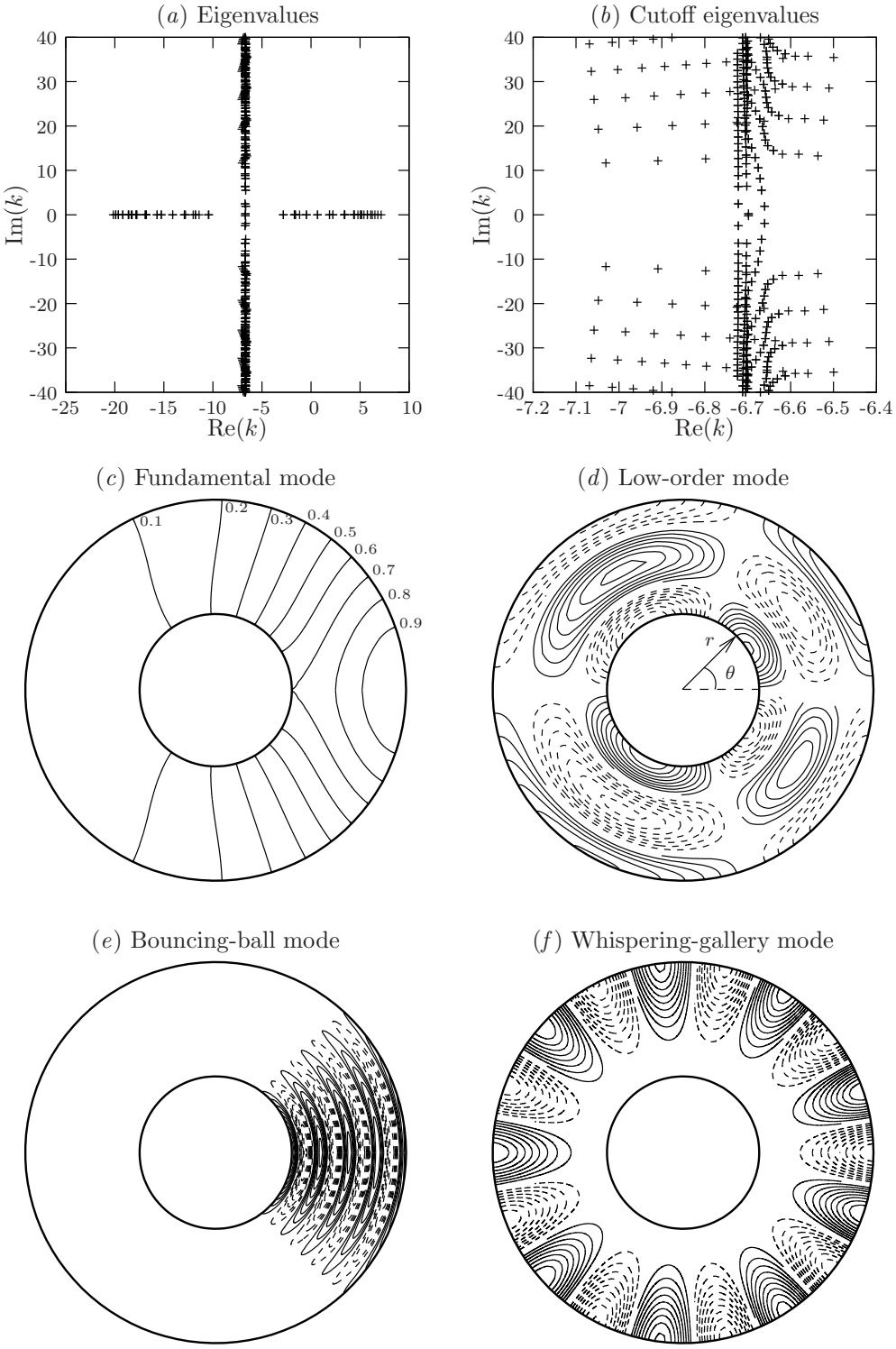

FIGURE 3. Upstream propagating modes in a hard-walled annular duct. Dashed lines indicate negative values. The axis orientation is shown in (d), giving the inside of the bend on the right and the mean flow into the page. $U_\infty = 0.5$, $\omega = 10$, $a_1/a_2 = 0.4$, and $\kappa = 0.1$.

and non-zero curvature, and can perhaps be associated with the asymmetric mean flow and asymmetric mode shapes, leading to slightly different Doppler shifts experienced by modes localised in different parts of the cross-section. Similar results can also be seen for hollow rather than annular duct cross-sections.

Figure 4(a) shows eigenvalues for a curved ($\kappa = 0.1$), lined ($Z = 2-\mathrm{i}$) hollow duct with mean flow ($U_\infty = 0.5$). The additional series of eigenvalues in the lower-half k-plane correspond to surface modes, exactly as for a straight duct (Rienstra 2003a; Brambley & Peake 2006). Figure 4(d) shows how such modes are strongly localised near the boundary, while figure 4(c) shows the upstream-propagating acoustic mode of the same order. This latter mode is a whispering-gallery mode, and while still being localised close to the outer boundary is noticeably more pervasive into the duct than the surface mode. (The true difference is that the mode in 4c decays algebraically away from the boundary, while that in 4d decays exponentially.) At the other extreme is the bouncing-ball mode shown in figure 4(b). These modes are similarly to the high-order modes in a hard-wall duct, except that for the lined duct there is very little oscillation at the duct wall. Figures 4(e, f) show the fundamental duct modes, and illustrate the dramatic asymmetry between upstream- and downstream-propagating modes. The upstream-propagating mode is removed from the boundary, similar to a mode with a pressure-release boundary condition, while the curvature biases the mode slightly to the inside of the bend (the right-hand side). The downstream-propagating mode, in contrast, is strongly localised on the outside of the bend, and is oscillating significantly on the duct boundary; it is very similar in form to a hard-wall duct mode.

Figure 5 shows how the axial wavenumbers k vary with the curvature κ. Note that owing to the left–right symmetry (in the sense of the cross-sections shown in figures 3 and 4) for $\kappa = 0$, two distinct modes with $\kappa \neq 0$ may merge into a double mode with $\kappa = 0$. As the curvature increases from zero, the first few downstream modes (on the right of figure 5b) become more damped. In contrast, the surface modes (i.e. the lower branch in the right half plane) for $k \lesssim 5$ become less damped, while most of the well cutoff acoustic modes (i.e. the ones in the line parallel to the vertical in figure 4a) maintain the same rate of decay, although their phase speed shifts slightly towards upstream.

Turning now to the RAE 2129 (hard-walled) duct described in §2, the cuton eigenvalues (i.e. those with real axial eigenvalue k) are plotted against the position along the duct centreline in figure 6, for a realistic aeroengine rotor-alone frequency. As can be seen, many modes which are cuton at the fan face ($s = 7.1$) will propagate all the way to the intake ($s = 0$). In figure 7 we plot the sound pressure level (SPL) of one such cuton mode (in the initial straight portion of the duct this corresponds to the $m = 24$ first radial order mode, a typical aeroengine rotor-alone mode), and in this case the amplitude varies rather little along the duct and the mode is concentrated close to the duct wall all the way along. The curvature does give an amplification of 4 dB to the mode, occurring on the inside of the left-most bend. For these parameters, there are also several duct modes which transition from cuton to cutoff within the duct, i.e. the sequence of real wavenumbers starting at the fan reaches a minimum value of s before turning round and moving back towards the fan (e.g. in figure 6 there are four modes which turn around near $s \approx 2$, etc.). These transitions correspond to wave reflection by the changing geometry and flow, and will be described in detail in the next section. The cutoff transition confines these modes to the fan end of the duct. The amplitude of one such mode is shown in figure 8 (in the initial straight portion of the duct corresponding to the $m = 24$ second radial order mode, a harmonic of a typical aeroengine rotor-alone mode), indicating the standing-wave pattern formed by the mode and its reflection between the fan and the transition point. This suggests the possibility of acoustic resonance, in which acoustic

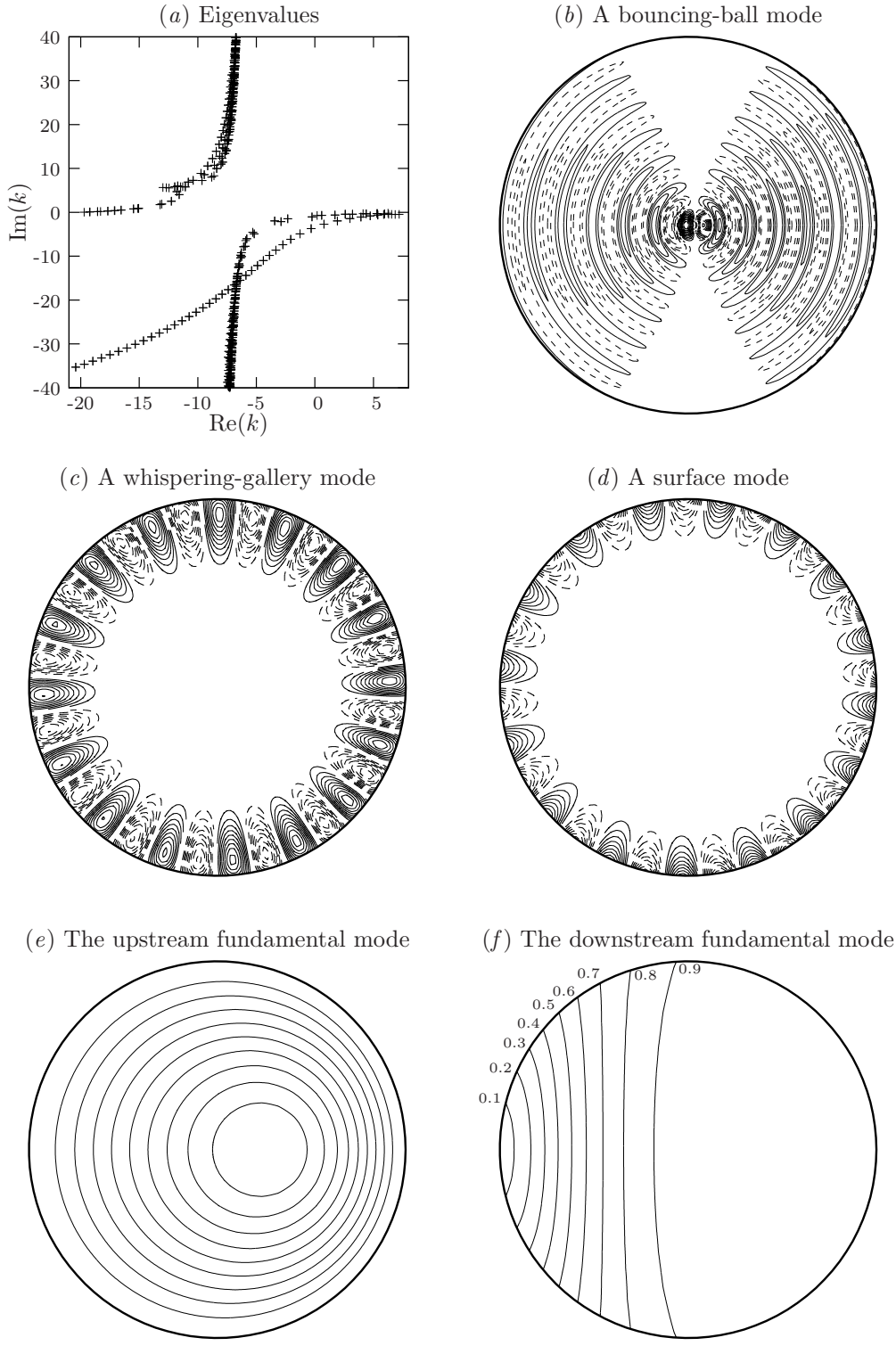

FIGURE 4. Results for a lined curved duct. Dashed lines indicate negative values. The axes are oriented as in figure 3. $U_\infty = 0.5$, $\kappa = 0.1$, $Z = 2 - \mathrm{i}$, and $\omega = 10$.

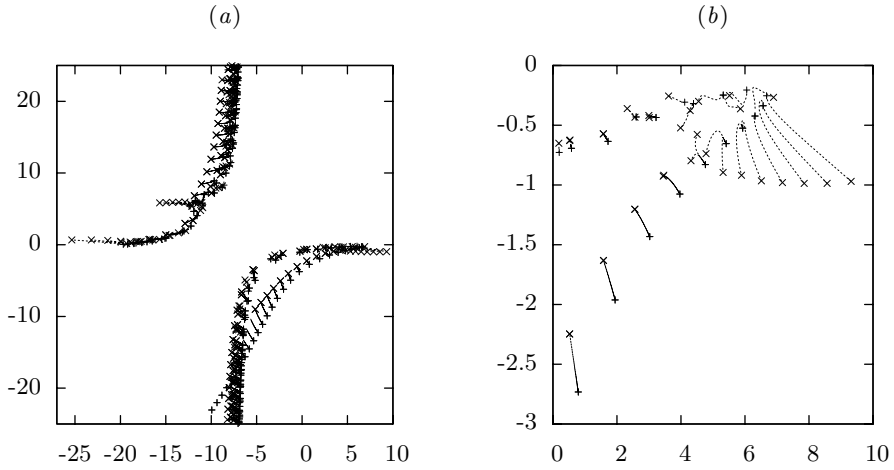

FIGURE 5. Graph showing the motion of eigenvalues in the k-plane due to varying the curvature from $\kappa = 0.0$ (+) to $\kappa = 0.4$ (×). $Z = 2 - \mathrm{i}$, $U_\infty = 0.5$, and $\omega = 10.0$. (b) A close up of the nearly cuton modes in (a).

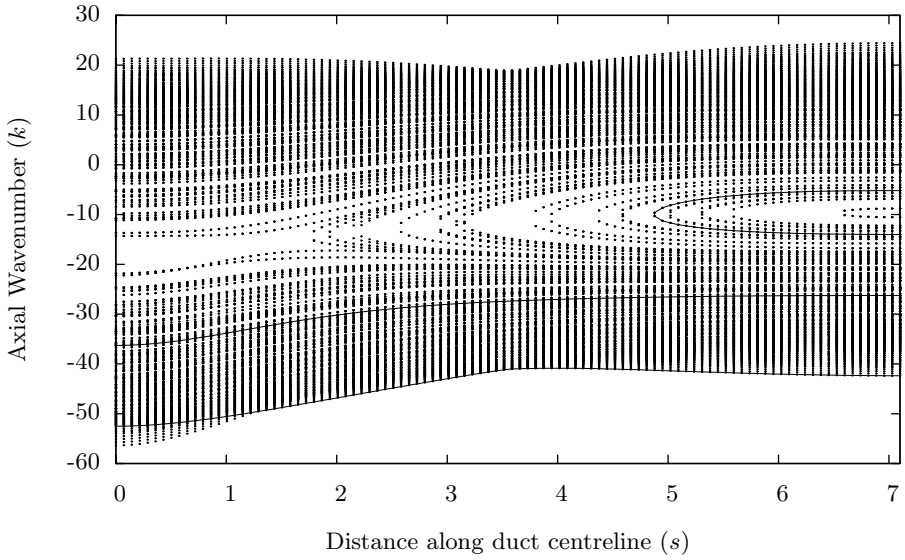

FIGURE 6. Real eigenvalues in the (hard-walled) RAE 2129 Inlet Diffuser shown in figure 2, for $\omega = 26.2$, giving $a_2^*\omega^*/C_\infty^* = 31.0$ at the fan face ($s = 7.1$). The mean flow has Mach number 0.5 at the intake ($s = 0$).

modes are trapped upstream of the fan by the cutoff transition and are prevented from propagating downstream by the swirl in the rotor–stator gap (see Cooper & Peake 2000).

6. Turning points and wave reflection

For a hard-walled duct the secularity condition (3.6) represents conservation of axial energy flux. Since a cuton mode has a non-zero energy flux and a cutoff mode has zero

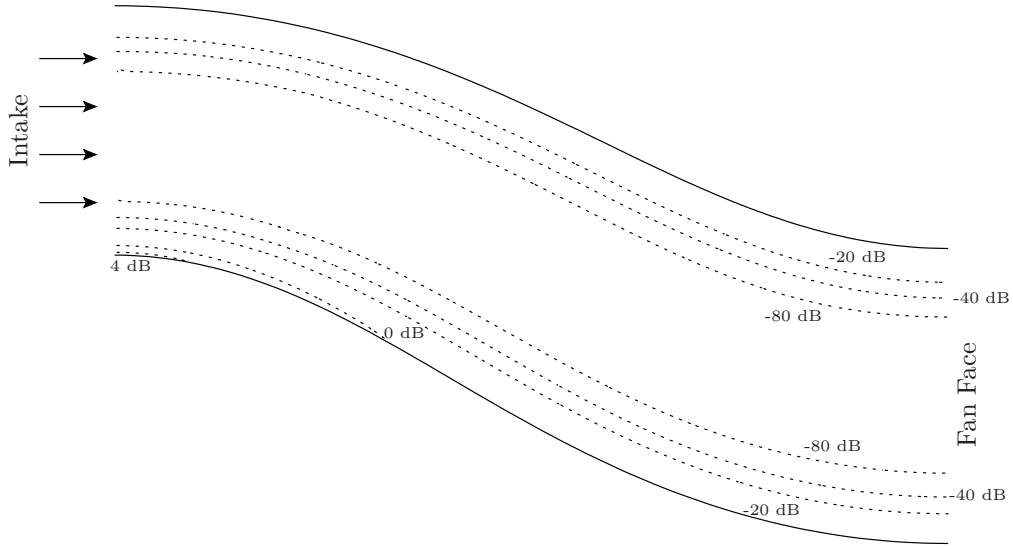

FIGURE 7. SPL for the first radial order, 24th azimuthal order mode propagating from right to left, normalized to give a maximum fan-face wall pressure of 0 dB. The axial wavenumber k for this mode is shown in figure 6 as the middle of the three solid lines.

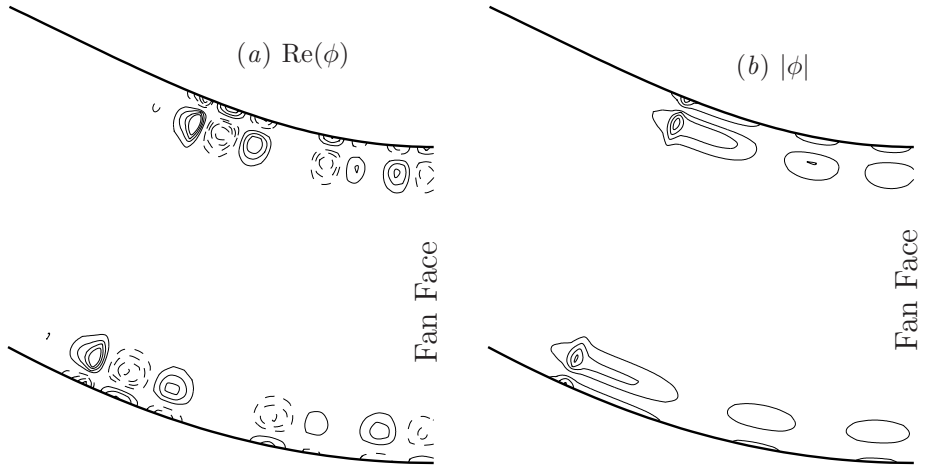

FIGURE 8. The second radial order, 24th azimuthal order mode propagating from the fan face (on the right) towards the intake (on the left), before being reflected by the duct geometry and propagating back towards the fan face. The axial wavenumbers k for these modes are shown as the upper solid line in figure 6. The incoming wave has unit maximum amplitude. Contours of $\mathrm{Re}(\phi)$ in (a) are at 0.5, 1.0, 1.5, and 2.0, with dashed lines indicating negative ϕ. Contours of $|\phi|$ in (b) are at 1.0, 2.0, 3.0, and 4.0.

energy flux, it is to be expected that the secularity condition breaks down in the neighbourhood of a cuton–cutoff transition. The secularity condition (3.6) becomes singular when $F(S) \to 0$, a so-called *turning point*. This is well understood in straight ducts (see, for example, Rienstra 2003*b*), and here we now derive the turning point behaviour incorporating curvature.

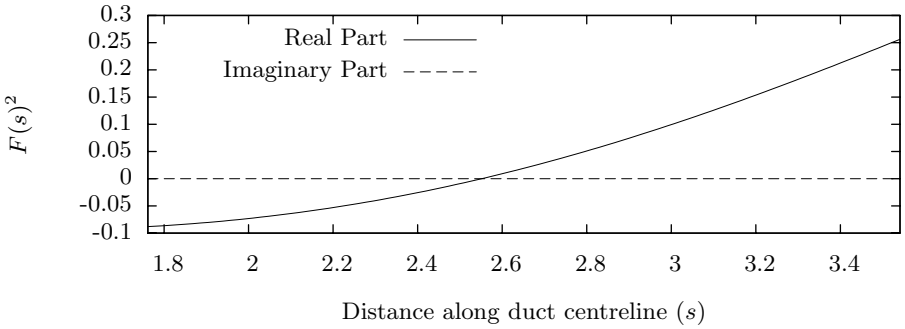

FIGURE 9. Graph showing the variation of $F(S)^2$ over a cutoff to cuton transition in the RAE 2129 Inlet Diffuser.

Define

$$G(S) = \int_0^{2\pi}\int_{a_1}^{a_2} \frac{D_0}{h_s}\hat{A_0}^2\left(1 - \frac{{U_0}^2}{{C_0}^2}\right) r\,\mathrm{d}r\,\mathrm{d}\theta,$$

so that $k = (F(S) - 1)/G(S)$. From previous studies on a straight duct (Rienstra 1999), we can expect that this transition occurs over a portion of the S-axis of length $O(\varepsilon^{2/3})$, and since $G(S)$ will vary little over this interval it follows that the change in k from real (cuton) to complex (cutoff) is associated with a change of sign of $F(S)^2$. Figure 9 shows the variation in $F(S)^2$ for a mode in the RAE 2129 duct that undergoes a cuton–cutoff transition; in the neighbourhood of the cutoff region, $F(S)^2$ is seen to be a linear function of S, and goes through zero as the mode transitions from cuton to cutoff.

The singularity in the secularity condition (3.6) is artificial and is due to the neglect of a term occurring at a higher power of ε. Including this term, the secularity condition becomes

$$\frac{\mathrm{d}}{\mathrm{d}S}\Big(FN^2\Big) + \mathrm{i}\varepsilon GN\frac{\mathrm{d}^2N}{\mathrm{d}S^2} = 0. \tag{6.1}$$

Let the turning point be at S_0, so that $F(S_0 + \Delta S) = \sqrt{a\Delta S}$ for some a. In what follows an inbound downstream propagating mode is considered (exactly the same analysis can be applied to an upstream propagating mode, for example as in the RAE 2129 duct), so that a is negative. By introducing the inner variable x, (6.1) becomes

$$N'' + 2\mathrm{i}\sqrt{x}N' + \frac{\mathrm{i}N}{2\sqrt{x}} = 0, \qquad \text{where} \qquad x = \Delta S\varepsilon^{-2/3}G^{-2/3}a^{1/3},$$

with branch cuts taken along the positive imaginary axis. This has leading-order solution

$$N = \big(A\mathrm{Ai}(-x) + B\mathrm{Bi}(-x)\big)\exp\left\{-\frac{2\mathrm{i}}{3}x^{3/2}\right\}.$$

Using asymptotic expansions of the Airy function for large $|x|$ (see Abramowitz & Stegun 1964, pp. 448–449), N has the large-x behaviour

$$N \sim \frac{\mathrm{e}^{\mathrm{i}\pi/4}}{2\sqrt{\pi}x^{1/4}}\left[(A - \mathrm{i}B)\exp\left\{-\frac{4\mathrm{i}}{3}x^{3/2}\right\} - \mathrm{i}(A + \mathrm{i}B)\right] \qquad \text{as } x \to \infty,$$

$$N \sim \frac{1}{2\sqrt{\pi}|x|^{1/4}}\left[A + 2B\exp\left\{\frac{4}{3}|x|^{3/2}\right\}\right] \qquad \text{as } x \to -\infty.$$

The outer solution to (3.6) about the singular point S_0 is

$$N = \begin{cases} \dfrac{N_0}{(a\Delta S)^{1/4}} & \text{for } S < S_0 \\ \\ \dfrac{TN_0 \mathrm{e}^{\mathrm{i}\pi/4}}{|a\Delta S|^{1/4}} & \text{for } S > S_0. \end{cases}$$

Expanding in terms of the inner variable x and matching with the inner solution gives $B = 0$ and $T = 1$. However, there is still an unmatched term as $x \to \infty$. This term is

$$\frac{A\mathrm{e}^{\mathrm{i}\pi/4}}{2\sqrt{\pi}x^{1/4}} \exp\left\{-\frac{4\mathrm{i}}{3}x^{3/2}\right\} \sim \frac{\mathrm{i}N_0}{\sqrt{F(S)}} \exp\left\{\frac{2\mathrm{i}}{\varepsilon}\int_{S_0}^{S} \frac{F(S')}{G(S')}\,\mathrm{d}S'\right\}.$$

The inbound downstream propagating mode has $k = (F(S)-1)/G(S)$. The corresponding upstream propagating mode would have $\tilde{k} = (-F(S)-1)/G = k - 2F(S)/G(S)$. Hence, the downstream propagating mode from the singular point would have the form

$$\frac{RN_0}{\sqrt{F(S)}} \exp\left\{-\frac{\mathrm{i}}{\varepsilon}\int_{S_0}^{S} \tilde{k}(S')\,\mathrm{d}S'\right\} = \exp\left\{-\frac{\mathrm{i}}{\varepsilon}\int_{S_0}^{S} k(S')\,\mathrm{d}S'\right\} \frac{RN_0}{\sqrt{F(S)}} \exp\left\{\frac{2\mathrm{i}}{\varepsilon}\int_{S_0}^{S} \frac{F(S')}{G(S')}\,\mathrm{d}S'\right\}.$$

This is exactly the solution needed to match with the extra term in the inner solution, provided $R = \mathrm{i}$.

This conclusion is exactly the same as was reached for a turning point in a straight duct by Rienstra (2003*b*). This is perhaps surprising, since within the inner region s varies by $O(\varepsilon^{-1/3})$, which is long compared with the local radius of curvature. The inner region is therefore strongly curved, albeit with a constant curvature, and so one might have expected a curvature-dependent reflection and transmission coefficient.

An example of the results of this matching behaviour is shown in figure 8, as previously discussed. Note that only the outer solution for ϕ is plotted in figure 8, and therefore a singularity at the reflection point is shown. This singularity is not physical, and is smoothed over by the inner Airy function solution. A method for obtaining a uniformly valid solution, incorporating both the inner and outer solutions, is given by Ovenden (2005), motivated by investigating cuton–cutoff transition near the ends of the duct (especially for civilian aeroengines, where the ducts are very short). This was not investigated further here, as the reflection points for a curved duct tend to occur in the centre of the duct, and away from this reflection point the accuracy of the outer solution is unaffected by the singularity. In particular, the reflection and transmission coefficients derived above, which are arguably the most important result of this section, are correct without needing to resort to a uniformly valid solution.

7. Ray theory for a hard-walled duct

We now investigate the high-frequency limit using ray theory. This will turn out not only to provide an asymptotic approximation for certain types of modes, but will also provide a more intuitive insight into why modes have the characteristics discovered above. We consider two different limiting cases. First, we are concerned with the fundamental modes, i.e. those which are very close to being plane waves. For a straight duct these

modes would have azimuthal order $m = 0$, and would be uniform across the duct cross-section. With wall curvature (and nonuniform mean flow), we see that the fundamental modes can be localised on one side of the bend or the other. In contrast, we consider second the limit of very high azimuthal order, and apply a known result of Babic & Buldyrev (1991) to determine the whispering-gallery modes.

In what follows, S will only occur as a parameter specifying which slice of the duct is being considered, and dependence on S will not be explicitly mentioned in the following equations. The gradient $\boldsymbol{\nabla}_\perp$ is used for the derivative in the cross-section of the duct, i.e. the r and θ directions only. We start off by introducing the ray ansatz for $A_0(r,\theta)$ by writing

$$A_0(r,\theta) = \frac{\mathcal{A}_0(r,\theta)}{\sqrt{h_s(r,\theta)D_0(r,\theta)}} \exp(-\mathrm{i}\omega\psi(r,\theta)) \; . \tag{7.1}$$

The reason for normalizing by the square root is to transform (3.3) into a form suitable for ray tracing (see A 6 in appendix A). We suppose that ω, the dimensionless frequency, is large, so that (7.1) corresponds to highly oscillatory modes, while ψ is $O(1)$. The corresponding unknown axial eigenvalue is $O(\omega)$, and so we write $k = \mu\omega$ with $\mu = O(1)$. Substituting (7.1) into (3.3) (or equivalently into A 6) and taking just the leading terms in ω, i.e. $O(\omega^2)$, we get

$$(\boldsymbol{\nabla}_\perp\psi)^2 = \alpha^2 \; , \qquad \alpha^2 = \frac{1}{{C_0}^2} - \frac{2\mu U_0}{h_s {C_0}^2} - \frac{\mu^2}{{h_s}^2}\left(1 - \frac{{U_0}^2}{{C_0}^2}\right) \; , \tag{7.2}$$

which is the standard ray-tracing result for propagation through a medium with nonuniform wavespeed $1/\alpha$ (this is a standard ray tracing derivation; see Babic & Buldyrev 1991, chapters 1 and 4 for details). Substituting (7.1) into (3.4), taking the hard-wall limit $Z_j \to \infty$, and taking just the leading terms in ω, i.e. $O(\omega)$, gives the boundary condition $\partial\psi/\partial r = 0$ at $r = a_j$. This gives simply normal reflection of a ray by the boundary (again, see Babic & Buldyrev 1991, chapter 4).

This result is quite important because it shows that, for large dimensionless frequencies ω, our problem for the curved duct with variable mean flow can be replaced by ray-tracing in two dimensions within a circular boundary with spatially varying sound speed $1/\alpha$. Note that the duct curvature and the duct radii affect α^2 through the mean flow terms (U_0, C_0 and D_0), as well as the curvature appearing in the metric factor h_s. In fact, it may be seen that α^2 only depends on $x = r\cos\theta$, the transverse position towards the inside or outside of the curve of the duct, and the position along the duct labelled by the slow axial coordinate S. The duct modes may therefore be thought of as bouncing around inside the cross-section of the duct, being reflected normally by the boundary, subject to a variable wave speed $1/\alpha$ that varies horizontally from the inside to the outside of the bend, but not vertically.

7.1. *Plane-wave localization*

The plane-wave fundamental modes for a straight duct are uniform across the duct cross-section. For a curved duct, some fundamental modes are shown in figures 3(c) and 4(e,f). As mentioned above, for these parameters the upstream-propagating modes are localized on the inside of the bend, while the downstream-propagating modes are localized on the outside. However, this is not always the case: figure 10 shows that, for $\kappa = 0.2$, $U_\infty = 0.5$, and $\omega = 31$ there are two upstream-propagating fundamental modes, one localized on the inside of the bend and one on the outside, with the downstream-propagating mode still localized on the outside. The wavenumbers for these modes are shown in figure 11, together with a left–right weighting

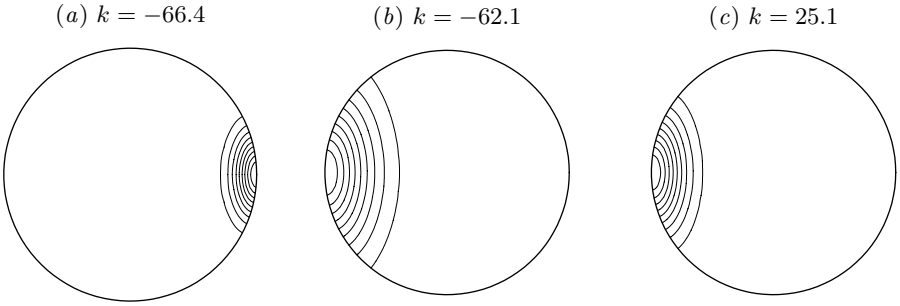

FIGURE 10. Fundamental modes, for a hard-wall duct with $\kappa = 0.2$, $U_\infty = 0.5$, and $\omega = 31$. The inside of the bend is on the right. (a) and (b) are upstream-propagating modes, while (c) is a downstream-propagating mode.

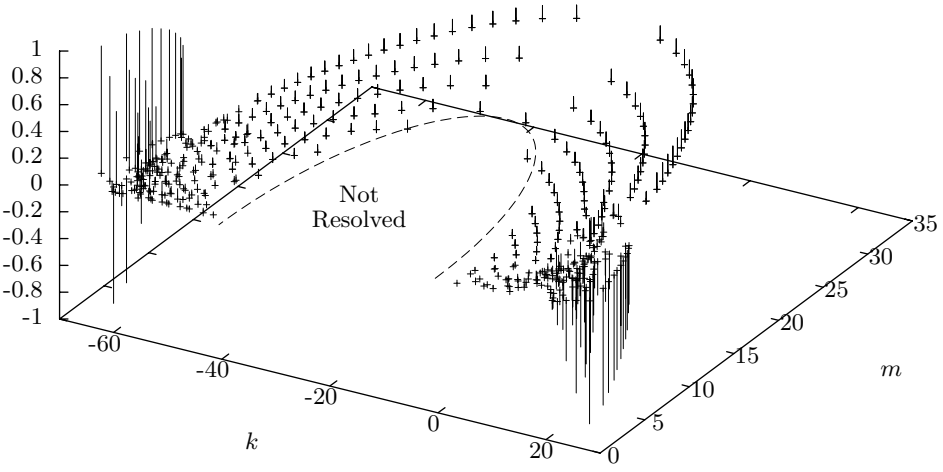

FIGURE 11. The wavenumbers k for propagating modes against their approximate azimuthal order m, for a hard-wall duct with $\kappa = 0.2$, $U_\infty = 0.5$, and $\omega = 31$. The vertical axis plots W_x, with modes localized on the inside and outside that have stalks extending upwards and downwards respectively. Only numerically resolved modes are shown ($n_r = 23$, $n_\theta = 131$); the curve denotes the unresolved region.

$$W_x = \frac{\int_0^{2\pi}\int_{a_1}^{a_2} r\cos(\theta)|A_0(r,\theta)|^2\, r\mathrm{d}r\mathrm{d}\theta}{\int_0^{2\pi}\int_{a_1}^{a_2} |A_0(r,\theta)|^2\, r\mathrm{d}r\mathrm{d}\theta}.$$

Modes which are highly localized on the left/right of the duct (i.e. on the outside/inside of the bend) have a value of W_x close to ∓ 1 respectively. The presence of a couple of upstream modes localized on the outside is clear in figure 11. The question is, therefore, what parameters influence the localization of duct modes?

In three dimensions, the fundamental modes may be thought of travelling nearly axially down the duct, reflecting occasionally from the duct boundary. In order to do this, the flow and the geometry must be such that a ray, having just reflected from the boundary, is driven back towards the boundary, as shown in figure 12(a). Figure 12(b) shows the corresponding projection of the rays onto the duct cross-section, as derived above. The dashed lines are where α^2 becomes negative, and the rays are restricted to regions where α^2 is positive.

A ray travelling purely axially at the local speed of sound along the duct at a fixed

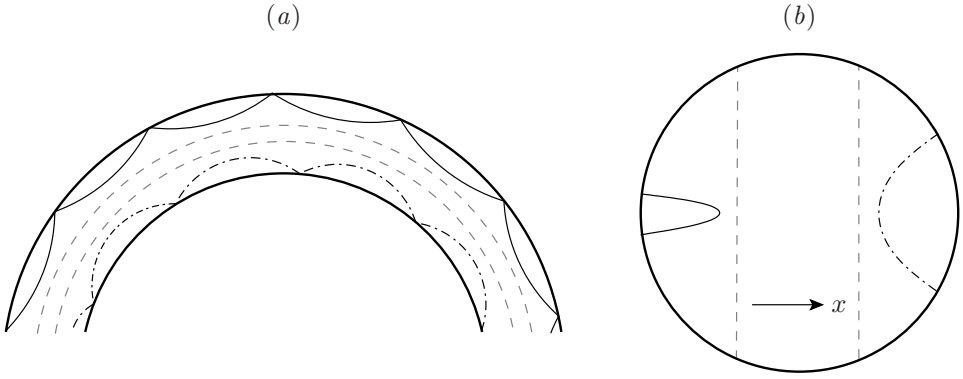

FIGURE 12. Schematic of localized fundamental rays. The dashed lines are where $\alpha^2 = 0$. (a) A projection of the three-dimensional rays onto a vertical plane, and (b) the corresponding projection onto the cross-sectional plane.

horizontal offset x from the duct centreline would give the ray-tracing parameter $\mu_\pm(x) = h_s/(U_0 \pm C_0)$, with + for downstream and − for upstream. Substituting $\mu_\pm(x)$ into (7.2) shows that $\alpha^2 = 0$ for each x, corresponding to the fact that such a ray is travelling completely in the axial direction, and therefore has no motion in the duct cross-section. Here, we are concerned with modes localized on the inside or outside boundary, and so (normalizing such that the duct radius is $a_2 = 1$) we are concerned only with the value of $\mu_\pm(x)$ at $x = 1$ (for the inside of the bend) and $x = -1$ (for the outside of the bend). Figure 13 shows the variation of α^2 across the duct for the four cases in which μ takes one of the values $\mu_+(\pm 1)$, $\mu_-(\pm 1)$. Figure 13(b) corresponds to figure 3, while figure 13(d) corresponds to figure 10. By perturbing the value of μ slightly from the values $\mu_\pm(\pm 1)$, it is possible that a small pocket of positive α^2 might be created close to the duct wall, and thus (provided the frequency is high enough) a localized mode on that boundary is possible. In order for a small perturbation to μ to lead to a localised mode on the boundary, $\alpha^2(x)$ must decrease away from that boundary. This is also the requirement that a ray having just reflected from the boundary is driven back towards the boundary (it is a standard ray-tracing result that rays bend towards regions with larger α, as may be seen by taking $\boldsymbol{\nabla}_\perp$ of the left-hand side of (7.2)). A change in the number of localized fundamental modes is therefore seen when the derivative of α^2 at $x = \pm 1$ changes sign. As an example, figure 13(a) demonstrates the possibility of a downstream fundamental mode localized on the outside of the bend and an upstream fundamental mode localized on the inside. Figures 13(b,d) both demonstrate the possibility of a downstream fundamental mode localized on the outside, and two upstream fundamental modes, one localized on the inside and one on the outside. Figure 13(c) demonstrates the possibility of both the downstream and upstream fundamental modes being localized on the outside of the bend.

In order to investigate which values of U_∞ and κ give rise to which types of localization behaviour, we will now look for a change in derivative of α^2 at $x = \pm 1$. Differentiating α^2 with respect to x gives

$$\frac{\partial \alpha^2}{\partial x} = \frac{(\gamma-1)\kappa {U_0}^2}{{C_0}^4 h_s} - \frac{2\kappa U_0 H(\gamma-1)\mu(2h_s - \mu U_0)}{{C_0}^4 {h_s}^3} - \frac{2\kappa\mu^2}{{h_s}^3}\left(1 - \frac{{U_0}^2}{{C_0}^2}\right), \tag{7.3}$$

and substituting $\mu = \mu_\pm(x) = h_s/(U_0 \pm C_0)$ gives

$$\frac{\partial \alpha^2}{\partial x} = \frac{\kappa}{h_s(U_0 \pm C_0)^2}\left[(\gamma-1)\frac{{U_0}^2}{{C_0}^2} \mp 4\frac{U_0}{C_0} - 2\right]. \tag{7.4}$$

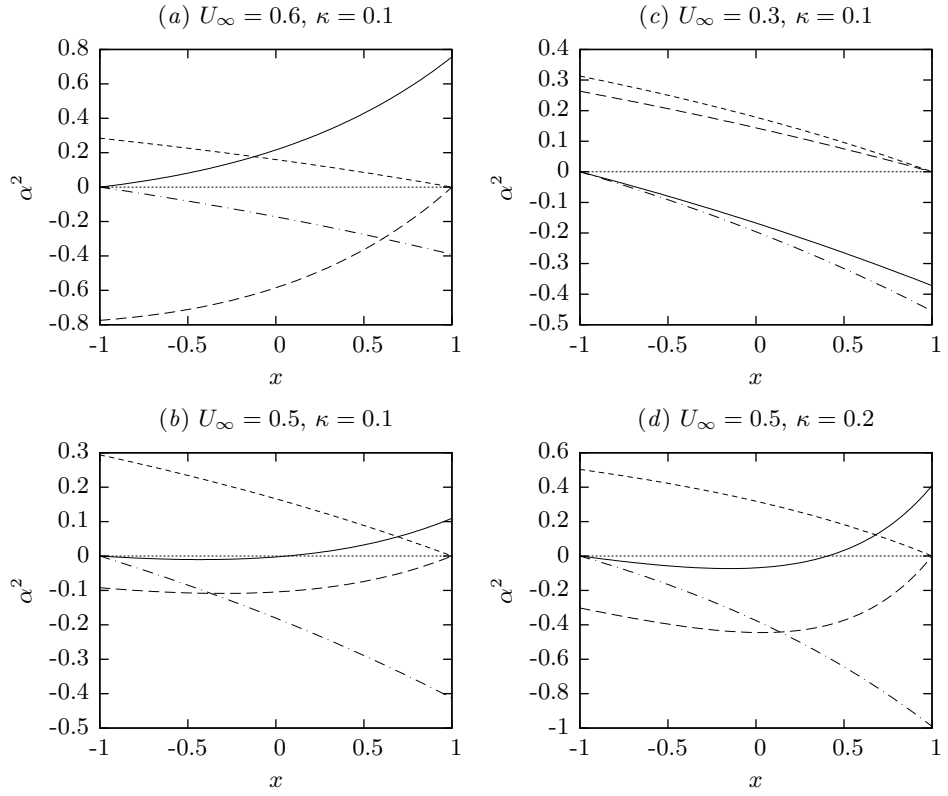

FIGURE 13. Graphs showing the variation in $\alpha^2(x)$ across the duct cross-section, for potential upstream- and downstream-propagating modes localized on the inside and outside of the duct bend. The solid line is the upstream outside mode (i.e. $\mu = \mu_-(-1)$), the long dashed line the upstream inside (i.e. $\mu = \mu_-(1)$), the short dashed line the downstream inside (i.e. $\mu = \mu_+(-1)$), and the dash–dot line the downstream outside (i.e. $\mu = \mu_+(1)$).

A sign change of $\partial\alpha^2/\partial x$ for a ray propagating axially down the duct is therefore given by a zero of the square brackets in (7.4). After some algebraic manipulation, this gives

$$U_0{}^2 = H\left(1 \pm \sqrt{\frac{2}{\gamma+1}}\right). \tag{7.5}$$

Note that the + solution of this (corresponding to a downstream-propagating mode) is very close to $U_0{}^2 = 2H$, at which point the mean density on the inside of the bend becomes zero.

Equation (7.5) may be evaluated to give κ in terms of U_∞, or U_∞ in terms of κ, for the critical parameters for which an upstream or downstream propagating mode ($-$ or $+$ in (7.5)) may be localized on the inside or outside of a bend (evaluating (7.5) at $x = 1$ or $x = -1$). Unfortunately, since $U_\dagger$ depends on both κ and U_∞ and is calculated numerically, (7.5) must in general be solved numerically. However, if the duct cross-sectional area is the same as far upstream, then it can be shown from (2.3) that $U_\dagger = U_\infty + O(\kappa^2)$. Hence, if the cross-sectional area is the same as far upstream and κ is small, (7.5) gives

$$\kappa = \frac{1}{x}\left(1 - U_\infty\left[H\left(1 \pm \sqrt{\frac{2}{\gamma+1}}\right)\right]^{-1/2}\right), \tag{7.6}$$

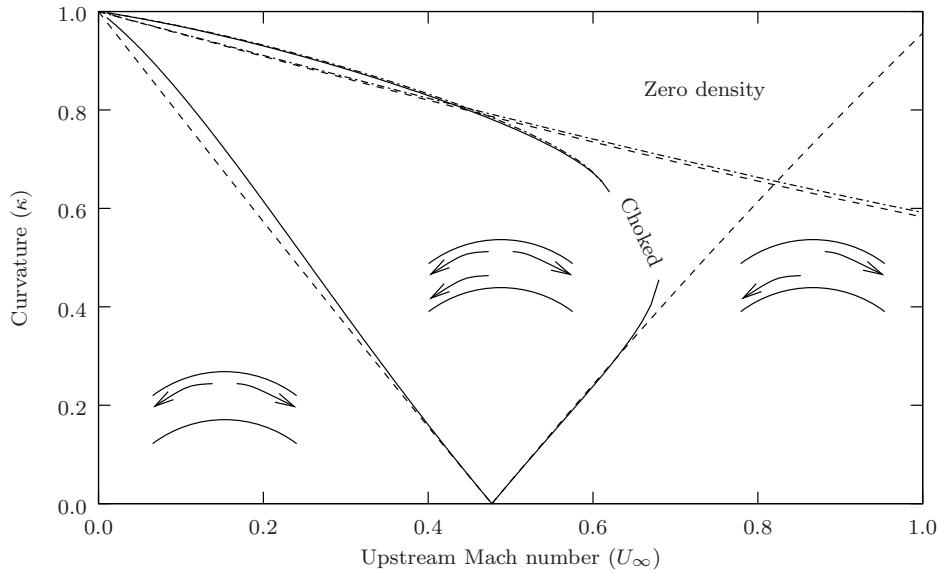

FIGURE 14. The different localization behaviours of plane waves for different upstream Mach numbers (U_∞) and curvatures (κ). The sketches show whether upstream and downstream modes localized on the inside and outside of the intake are possible, with downstream being the right–facing arrow. Solid lines are numerical results from (7.5), and dashed lines are asymptotic results from (7.6). The two dash–dot lines (one numerical and one asymptotic) are where ${U_0}^2 = 2H$, for which the density on the inside of the bend becomes zero.

with x being either $+1$ or -1 for the inside or outside of the bend. Here H is given by (2.1) upstream.

Figure 14 plots the small-curvature asymptotics given by (7.6) and the numerically calculated solutions of (7.5). The numerically generated solutions stop around $U_\infty = 0.65$, since for these parameters the duct is choked; i.e. there is no solution to (2.3) for $U_\dagger$ that gives the required mass flow rate.

Interestingly, the boundaries between the different behaviours of the upstream fundamental mode intersect at $\kappa = 0$, as shown in figure 14. At this point, the small-curvature asymptotics give the exact answer (assuming the duct cross-sectional area is the same as far upstream), and rearranging (7.6) gives the upstream Mach number for which this occurs as

$$U_\infty = \frac{2}{\gamma - 1}\left(\sqrt{\frac{\gamma+1}{2}} - 1\right).$$

For $\gamma = 1.4$, as used for all the examples presented here, this gives $U_\infty \approx 0.477$. This means that, for U_∞ close to this value (and $U_\infty = 0.5$ has been used for most examples presented here) for all but very small curvatures it is possible for both the upstream localized modes to be present. Indeed, this can be seen in Figure 10, where both inside- and outside-localised upstream modes are shown.

For low Mach number flows, the geometry keeps both upstream and downstream modes localized on the outside of the bend. This is exactly the result seen by Felix & Pagneux (2004). However, different behaviour is seen for larger Mach number flows. For large Mach number flows, the mean flow is fastest on the inside of the bend and slowest on the outside, giving a refraction effect which curves upstream-propagating rays towards the inside of the bend and downstream-propagating rays towards the outside. Hence, as the

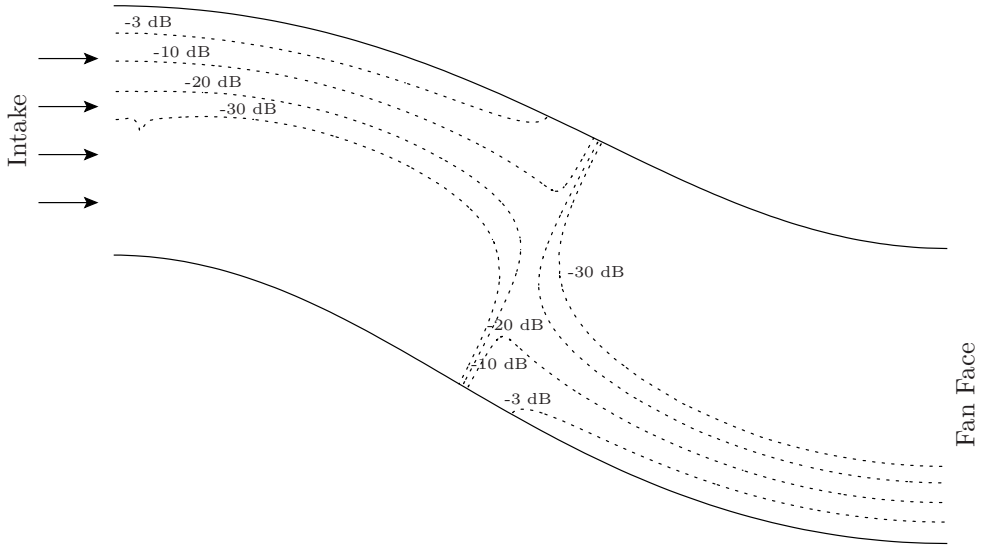

FIGURE 15. SPL for the plane-wave mode propagating from right to left, normalized to give a maximum fan-face wall pressure of 0 dB. The axial wavenumber k for this mode is shown in figure 6 as the bottom of the three solid lines.

Mach number is increased from zero, the upstream mode first becomes present on the inner wall, and then disappears from the outside as the Mach number is increased further. Increasing the curvature makes this effect more pronounced. This case is similar to the unsteady flow through a loaded cascade considered by Atassi, Fang & Patrick (1993), in which upstream propagating waves can propagate along the suction surface of the blade (corresponding to the inside of our bend) and become blocked if the mean flow becomes locally close to sonic, giving increased local amplitudes on the suction surface.

Figure 15 gives an example of an upstream-propagating plane wave in the RAE 2129 duct, in a similar manner to figure 7. In this case, the mode is always localized on the outside of the bends, and becomes a straight-duct plane wave at the midpoint of the intake where the curvature passes through zero. On the right (fan-end) of the duct only this localization is possible. On the left (intake-end) a mode localized on the inside of the bend is also possible, but is not excited.

The validity of the results of this section requires the frequency ω to be high enough. For the relatively low frequency $\omega = 10$, as in figures 3 and 4, no upstream modes localized on the outside can be found. However, for the high frequency $\omega = 31$, the ray-theory prediction of inside and outside upstream fundamental modes presented in figure 14 is confirmed in figure 11.

While the results presented here have been for a duct with the same cross-section as far upstream, (7.5) is still valid even if this is not the case. The small-κ asymptotics of (7.6) do require this restriction, however.

7.2. *Whispering-gallery modes*

Keller & Rubinow (1960) used ray theory to construct a method for determining the eigenvalues of the Helmholtz equation in certain closed domains containing a uniform acoustic medium. Their procedure was adapted by Babic & Buldyrev (1991) to domains with a varying sound speed. We now make use of Babic & Buldyrev's procedure to obtain analytically-based approximations for the eigenvalues of our curved duct at high frequency and high azimuthal order for the case of hard duct walls.

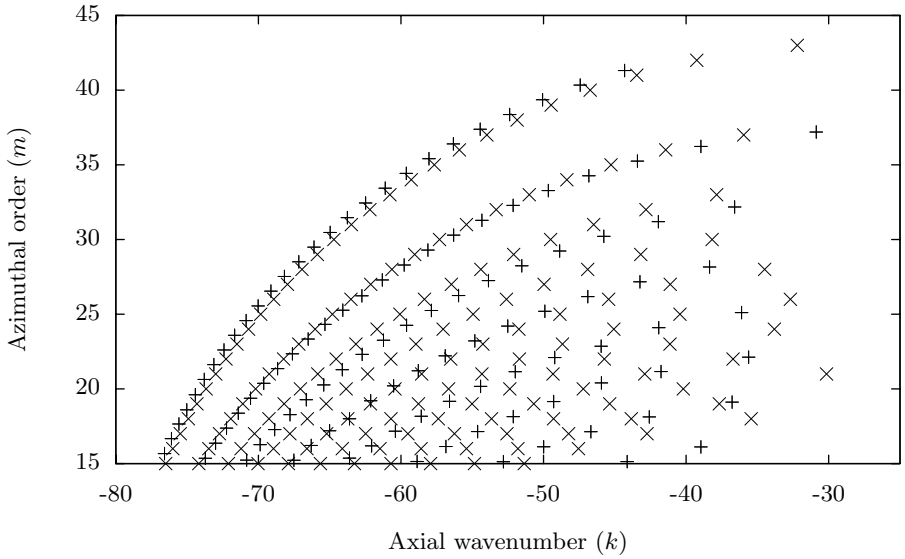

FIGURE 16. Comparison of ray-tracing asymptotics (×) with numerical results (+). $U_\infty = 0.5$, $\kappa = 0.1$ and $\omega = 40$.

One key step in the Keller & Rubinow procedure is the determination of the shape of a caustic surface inside the domain, which provides an envelope for all possible ray directions. In the case of a circular domain with a uniform medium these caustics are simply concentric circles, whose radii are related to the allowed eigenvalues of the problem. However, for our equivalent variable sound speed it does not appear possible to determine the shape of this caustic in general, but analytical progress can be made for so-called *whispering-gallery* modes. Whispering-gallery modes consist of rays running close to the boundary, bouncing a large number of times at very short intervals. A typical modal shape is shown in figure 4(c).

Babic & Buldyrev (1991) determined an asymptotic expression for the eigenvalues of whispering-gallery modes of a circle with nonuniform sound speed. These modes are parameterized by two integers: $m \gg 1$, the azimuthal order, and $j = 1, 2, \ldots$, the radial order. For the case of a curved duct, with the effective sound speed given by (7.2), their analysis gives (see Babic & Buldyrev 1991, §5.3)

$$k_{jm} = \frac{\pi\mu}{I_1(a_2)} \left\{ 2m + I_2(a_2) \left[\frac{9m}{4I_1(a_2)} \big(j - 3/4\big)^2 \right]^{1/3} \right\}, \tag{7.7}$$

where

$$I_1(r) = \int_0^{2\pi} \alpha \, r \mathrm{d}\theta, \quad I_2(r) = \int_0^{2\pi} \alpha^{1/3} \left(\frac{1}{r} + \frac{1}{2\alpha^2} \frac{\partial \alpha^2}{\partial r} \right)^{2/3} r \mathrm{d}\theta, \quad \frac{\partial \alpha^2}{\partial r} = \cos\theta \frac{\partial \alpha^2}{\partial x},$$

with $\partial\alpha^2/\partial x$ given in (7.3). This expression is valid for both annular and hollow ducts; because the rays are bouncing around the outer boundary, the inner boundary plays no part. Note that (7.7) gives $k_{jm}(\mu)$ implicitly as a function of $\mu \equiv k_{jm}/\omega$, and an iterative method was therefore needed to find the axial wavenumber k_{jm} for a specified value of ω. Figure 16 shows the results of the ray tracing asymptotics against numerically calculated eigenvalues. A frequency of $\omega = 40$ was used for the comparison, so as to allow high azimuthal order modes to be cuton. The results are plotted against the azimuthal-order

m so the individual modes can be distinguished. The agreement is seen to be reasonable, especially for nearly cutoff large-m modes, as is to be expected from using large m asymptotics.

8. Concluding remarks

In this paper we have considered the propagation of acoustic waves along a curved duct carrying mean potential flow. The wall radii, impedance of the acoustic lining, and curvature of the duct centreline may vary slowly along the duct, allowing application of an asymptotic multiple-scales analysis. Our general results have not relied on any assumption of weak curvature. We have seen that the spectrum of local eigenmodes is more complicated than in the straight-duct case, due to the fundamental asymmetry between upstream and downstream propagating modes. For the plane-wave fundamental modes in a hard-wall duct, this asymmetry has been classified into different regions of parameter space, depending on the local curvature and the upstream Mach number. This asymmetry is even more pronounced when an acoustic lining is present. In contrast, our closed-form expression for the variation of the slowly varying amplitude is very similar in form to the straight-duct case, possibly due to its connection with the energy flux along the duct. This similarity even extends to cuton–cutoff turning points, for which the straight-duct solution is recovered despite the duct being significantly curved (albeit with constant curvature) on the inner asymptotic region.

Throughout this paper we have assumed an inviscid mean flow, and indeed in most circumstances this is a valid assumption. In some cases, however, particularly for strongly curved ducts and high Mach number mean flows, it is possible for the viscous boundary layer along the duct wall to separate. This possibility has been neglected here. However, assuming the boundary layer remains attached to the duct walls, it is expected that the inviscid assumption will be acceptable.

The pseudospectral eigenvalue solver is sufficiently general to allow straightforward extension of our solution to more complicated geometries; for example, to the curved-duct version of Rienstra's (2003*b*) solution for a duct of arbitrary slowly varying cross-section. Another possible extension of this work would be to relax the restriction that the duct centreline is planar. This means that as well as a nonzero slowly varying curvature, the duct centreline would possess a slowly varying torsion $\tau(S)$. Germano (1982) showed how the coordinate system can be modified to account for this effect, simply by replacing the cross-sectional polar angle θ by

$$\theta + \frac{1}{\varepsilon}\int_0^S \tau(S')\,\mathrm{d}S' \,,$$

which yields an orthogonal coordinate system which effectively twists with the duct centreline. For zero mean flow the effect of torsion can therefore be included as a very simple modification of the results given in §3. For nonzero mean flow, however, the cross-sectional components V, W become $O(1)$ when $\tau \neq 0$, rather than $O(\varepsilon)$ when $\tau = 0$, and this would lead to significant, but perhaps not intractable, complication.

This work has been supported by an EPSRC CASE award from Rolls-Royce. Helpful discussions with Dr S. W. Rienstra are gratefully acknowledged.

Appendix. Details of the multiple-scales derivation

We consider a small perturbation $(\boldsymbol{u}, \rho, p)$ with time dependence $\exp\{\mathrm{i}\omega t\}$ to the steady mean flow $(\boldsymbol{U}, D, P)$. We neglect vortical and entropic perturbations, and introduce a scalar potential $\boldsymbol{u} = \boldsymbol{\nabla}\phi$. Our starting point is (3.1), the equation for the unsteady linearized flow due to Goldstein (1978)

$$\frac{\mathrm{D}}{\mathrm{D}t}\left(\frac{1}{C^2}\frac{\mathrm{D}\phi}{\mathrm{D}t}\right) - \frac{1}{D}\boldsymbol{\nabla}\cdot\left(D\boldsymbol{\nabla}\phi\right) = 0, \qquad\qquad p = C^2\rho = -D\frac{\mathrm{D}\phi}{\mathrm{D}t}, \tag{A 1}$$

where $\mathrm{D}/\mathrm{D}t = \mathrm{i}\omega + \boldsymbol{U}\cdot\boldsymbol{\nabla}$ and $C^2 = D^{\gamma-1}$, and (3.2), the Myers (1980) boundary condition for a lined duct,

$$\mathrm{i}\omega\boldsymbol{n}\cdot\boldsymbol{\nabla}\phi = \Big\{\mathrm{i}\omega + \boldsymbol{U}\cdot\boldsymbol{\nabla} - \big[(\boldsymbol{n}\cdot\boldsymbol{\nabla})\boldsymbol{U}\big]\cdot\boldsymbol{n}\Big\}(p/Z_j) \qquad \text{on } r = a_j(S) \text{ for } j = 1, 2\ , \tag{A 2}$$

where $Z_{1,2}(S)$ are the wall impedances and $\boldsymbol{n}$ is the corresponding wall normal pointing out of the fluid.

We pose the multiple-scales WKB ansatz (see for instance Hinch 1991, chapter 7)

$$\phi = A(S, r, \theta)\exp\left\{\mathrm{i}\omega t - \frac{\mathrm{i}}{\varepsilon}\int_0^S k(S')\,\mathrm{d}S'\right\}\ . \tag{A 3}$$

For brevity, define the linear operators

$$\Lambda = \omega - \frac{kU_0}{h_s} \qquad\qquad \mathcal{D} = \frac{U_0}{h_s}\frac{\partial}{\partial S} + V_1\frac{\partial}{\partial r} + W_1\frac{1}{r}\frac{\partial}{\partial\theta},$$

so that $\mathrm{D}/\mathrm{D}t = \mathrm{i}\Lambda + \varepsilon\mathcal{D} + O(\varepsilon^2)$. Substituting (A 3) into (A 1) gives

$$\begin{aligned}\frac{1}{h_sD_0}\left[\frac{1}{r}\frac{\partial}{\partial r}\left(rh_sD_0\frac{\partial A}{\partial r}\right) + \frac{1}{r^2}\frac{\partial}{\partial\theta}\left(h_sD_0\frac{\partial A}{\partial\theta}\right)\right] + \left(\frac{\Lambda^2}{{C_0}^2} - \frac{k^2}{{h_s}^2}\right)A \\ = \mathrm{i}\varepsilon\left[\frac{2\Lambda}{{C_0}^2}\mathcal{D}A + A\mathcal{D}\left(\frac{\Lambda}{{C_0}^2}\right) + \frac{2k}{{h_s}^2}\frac{\partial A}{\partial S} + \frac{A}{h_sD_0}\frac{\partial}{\partial S}\left(\frac{D_0k}{h_s}\right)\right] + O(\varepsilon^2),\end{aligned} \tag{A 4}$$

subject to the boundary conditions (from A 2)

$$\begin{aligned}&\pm\frac{\partial A}{\partial r} - \frac{\Lambda^2D_0}{\mathrm{i}\omega Z_j}A \\ &= -\varepsilon\left[\pm\frac{\mathrm{i}k}{{h_s}^2}\frac{\mathrm{d}a_j}{\mathrm{d}S}A + \frac{1}{A}\mathcal{D}\left(\frac{\Lambda D_0A^2}{\omega Z_j}\right) + \frac{D_0\Lambda}{Z_j\omega}\left(\frac{\mathrm{d}a_j}{\mathrm{d}S}\frac{\partial}{\partial r}\left(\frac{U_0}{h_s}\right) - \frac{\partial V_1}{\partial r}\right)A\right] + O(\varepsilon^2)\end{aligned} \tag{A 5}$$

at $r = a_j$, where the positive sign is taken for $j = 2$ and the negative sign for $j = 1$.

For ray-tracing applications, (A 4) may be rearranged to give

$$\begin{aligned}\frac{1}{r}\frac{\partial}{\partial r}\left(r\frac{\partial A}{\partial r}\right) + \frac{1}{r^2}\frac{\partial^2A}{\partial\theta^2} - \frac{\kappa}{h_s}\left(1 + \frac{{U_0}^2}{{C_0}^2}\right)\left[\frac{\partial A}{\partial r}\cos\theta - \frac{1}{r}\frac{\partial A}{\partial\theta}\sin\theta\right] \\ + \left[\frac{\omega^2}{{C_0}^2} - \frac{2\omega U_0k}{h_s{C_0}^2} - \frac{k^2}{{h_s}^2}\left(1 - \frac{{U_0}^2}{{C_0}^2}\right)\right]A \\ = \frac{\mathrm{i}\varepsilon}{h_sD_0A}\left[h_sD_0\mathcal{D}\left(\frac{A^2\Lambda}{{C_0}^2}\right) + \frac{\partial}{\partial S}\left(\frac{D_0kA^2}{h_s}\right)\right],\end{aligned}$$

and then, by making the substitution $\psi = \sqrt{h_s D_0} A$,

$$\frac{1}{r}\frac{\partial}{\partial r}\left(r\frac{\partial \psi}{\partial r}\right) + \frac{1}{r^2}\frac{\partial^2 \psi}{\partial r^2} + \left[\frac{\omega^2}{{C_0}^2} - \frac{2\omega U_0 k}{h_s {C_0}^2} - \frac{k^2}{{h_s}^2}\left(1 - \frac{{U_0}^2}{{C_0}^2}\right) + \frac{\kappa^2}{4{h_s}^2}\left(1 + 4\frac{{U_0}^2}{{C_0}^2} + (2\gamma - 3)\frac{{U_0}^4}{{C_0}^4}\right)\right]\psi = \frac{\mathrm{i}\varepsilon}{\psi}\left[h_s D_0 \mathcal{D}\left(\frac{\psi^2 \Lambda}{h_s D_0 {C_0}^2}\right) + \frac{\partial}{\partial S}\left(\frac{k\psi^2}{{h_s}^2}\right)\right]. \quad (A\,6)$$

Returning to (A 4) and expanding $A = A_0 + \varepsilon A_1 + O(\varepsilon^2)$ gives, to leading order,

$$\mathcal{L}A_0 \equiv \frac{1}{h_s D_0}\left[\frac{1}{r}\frac{\partial}{\partial r}\left(r h_s D_0 \frac{\partial A_0}{\partial r}\right) + \frac{1}{r^2}\frac{\partial}{\partial \theta}\left(h_s D_0 \frac{\partial A_0}{\partial \theta}\right)\right] + \left(\frac{\Lambda^2}{{C_0}^2} - \frac{k^2}{{h_s}^2}\right)A_0 = 0\,, \quad (A\,7)$$

subject to the boundary conditions (from A 5)

$$\frac{\partial A_0}{\partial r} = \pm \frac{\Lambda^2 D_0}{\mathrm{i}\omega Z_j} A_0 \qquad \text{at } r = a_j, \qquad j = 1, 2. \quad (A\,8)$$

Equations (A 7) and (A 8) are exactly the leading order equations (3.3) and (3.4).

At $O(\varepsilon)$, (A 4) gives

$$\mathcal{L}A_1 = \frac{\mathrm{i}}{h_s D_0 A_0}\left[h_s D_0 \mathcal{D}\left(\frac{{A_0}^2 \Lambda}{{C_0}^2}\right) + \frac{\partial}{\partial S}\left(\frac{D_0 k {A_0}^2}{h_s}\right)\right], \quad (A\,9)$$

where $\mathcal{L}$ is the operator defined in (A 7), subject to the boundary conditions (from A 5)

$$\pm\frac{\partial A_1}{\partial r} - \frac{\Lambda^2 D_0}{\mathrm{i}\omega Z_j}A_1 = \mp\frac{\mathrm{i}k}{{h_s}^2}\frac{\mathrm{d}a_j}{\mathrm{d}S}A_0 - \frac{1}{A_0}\mathcal{D}\left(\frac{\Lambda D_0 {A_0}^2}{\omega Z_j}\right) - \frac{D_0 \Lambda}{Z_j \omega}\left(\frac{\mathrm{d}a_j}{\mathrm{d}S}\frac{\partial}{\partial r}\left(\frac{U_0}{h_s}\right) - \frac{\partial V_1}{\partial r}\right)A_0 \quad (A\,10)$$

at $r = a_j$, with $\pm$ being $+$ at $r = a_2$ and $-$ at $r = a_1$ (this convention will be assumed from here on). Note that, by using integration by parts to move derivatives from A_1 onto A_0 and the fact that $\mathcal{L}A_0 = 0$,

$$\int_0^{2\pi}\int_{a_1}^{a_2} A_0 \mathcal{L}(A_1) h_s D_0 \, r\mathrm{d}r\mathrm{d}\theta = \left[\int_0^{2\pi}\left(A_0\frac{\partial A_1}{\partial r} - A_1\frac{\partial A_0}{\partial r}\right) r h_s D_0 \, \mathrm{d}\theta\right]_{a_1}^{a_2},$$

where the $[\cdots]_0^{2\pi}$ terms that would have appeared above are zero owing to 2π periodicity. Multiplying (A 9) by $A_0 h_s D_0 r$ and integrating over r and θ, and then substituting for $\partial A_0/\partial r$ and $\partial A_1/\partial r$ using the boundary conditions (A 8) and (A 10) therefore gives

$$-\mathrm{i}\int_0^{2\pi}\left[\left(\frac{k}{{h_s}^2}\frac{\mathrm{d}a_j}{\mathrm{d}S}{A_0}^2 \pm \mathcal{D}\left(\frac{\Lambda D_0 {A_0}^2}{\mathrm{i}\omega Z_j}\right) \pm \frac{D_0 \Lambda {A_0}^2}{\mathrm{i}\omega Z_j}\left(\frac{\mathrm{d}a_j}{\mathrm{d}S}\frac{\partial}{\partial r}\left(\frac{U_0}{h_s}\right) - \frac{\partial V_1}{\partial r}\right)\right) r h_s D_0\right]_{a_1}^{a_2}\mathrm{d}\theta = \mathrm{i}\int_0^{2\pi}\int_{a_1}^{a_2} r h_s D_0 \mathcal{D}\left(\frac{{A_0}^2 \Lambda}{{C_0}^2}\right) + r\frac{\partial}{\partial S}\left(\frac{D_0 k {A_0}^2}{h_s}\right)\mathrm{d}r\mathrm{d}\theta. \quad (A\,11)$$

Note that, since $\boldsymbol{\nabla}\cdot(D\boldsymbol{U}) = 0$, for any function $f(S, r, \theta)$, $\boldsymbol{\nabla}\cdot(D\boldsymbol{U}f) = \varepsilon D\mathcal{D}f$, and hence

$$r h_s D_0 \mathcal{D}f = r\frac{\partial}{\partial S}(D_0 U_0 f) + \frac{\partial}{\partial r}(r h_s D_0 V_1 f) + \frac{\partial}{\partial \theta}(h_s D_0 W_1 f).$$

Using this to eliminate the $\mathcal{D}$ operator from (A 11), substituting $V_1 = (\mathrm{d}a_j/\mathrm{d}S)(U_0/h_s)$

from the mean flow boundary conditions at $r = a_j$ and rearranging gives

$$Q_1 + Q_2 + \int_0^{2\pi}\int_{a_1}^{a_2} \frac{\partial}{\partial S}\left(\frac{D_0 k {A_0}^2}{h_s} + \frac{{A_0}^2 D_0 U_0 \Lambda}{{C_0}^2}\right) r\mathrm{d}r\mathrm{d}\theta + \int_0^{2\pi}\left[r\frac{\mathrm{d}a_j}{\mathrm{d}S}\left(\frac{D_0 k {A_0}^2}{h_s} + \frac{{A_0}^2 D_0 U_0 \Lambda}{{C_0}^2}\right)\right]_{a_1}^{a_2}\mathrm{d}\theta = 0, \quad \text{(A 12)}$$

where, setting $f_j = \Lambda {D_0}^2 {A_0}^2 r/(\mathrm{i}\omega Z_j)$,

$$Q_j = \int_0^{2\pi}\left[\frac{\partial}{\partial S}(U_0 f_j) + \frac{\partial}{\partial r}(h_s V_1 f_j) + h_s f_j\left(\frac{\mathrm{d}a_j}{\mathrm{d}S}\frac{\partial}{\partial r}\left(\frac{U_0}{h_s}\right) - \frac{\partial V_1}{\partial r}\right)\right]\mathrm{d}\theta\bigg|_{r=a_j},$$

where a term involving W_1 integrates to give zero owing to 2π periodicity. Expanding the $\partial/\partial r$ terms and again using $V_1 = (\mathrm{d}a_j/\mathrm{d}S)(U_0/h_s)$ gives

$$\begin{aligned} Q_j &= \int_0^{2\pi}\left[\frac{\partial}{\partial S}(U_0 f_j) + \frac{\mathrm{d}a_j}{\mathrm{d}S}\frac{\partial}{\partial r}(U_0 f_j)\right]\mathrm{d}\theta\bigg|_{r=a_j} \\ &= \frac{\mathrm{d}}{\mathrm{d}S}\underbrace{\left(\int_0^{2\pi}\frac{U_0 \Lambda {D_0}^2 {A_0}^2}{\mathrm{i}\omega Z_j}\, r\mathrm{d}\theta\bigg|_{r=a_j}\right)}_{I_j(S)}. \end{aligned} \quad \text{(A 13)}$$

Hence, (A 12) may be rearranged, moving the $\partial/\partial S$ derivative to the other side of the integrals as we just have done for Q_j above, to finally get

$$\frac{\mathrm{d}}{\mathrm{d}S}\left(I_1 + I_2 + \underbrace{\int_0^{2\pi}\int_{a_1}^{a_2} D_0 {A_0}^2\left(\frac{\omega U_0}{{C_0}^2} + \frac{k}{h_s}\left(1 - \frac{{U_0}^2}{{C_0}^2}\right)\right) r\mathrm{d}r\mathrm{d}\theta}_{F(S)}\right) = 0,$$

with $I_{1,2}$ defined in (A 13). Setting $A_0(S, r, \theta) = \hat{A}_0(S, r, \theta)N(S)$ gives the secularity condition as written in (3.6)

REFERENCES

Abramowitz, M. & Stegun, I. A. 1964 *Handbook of Mathematical Functions*, 9th edn. Dover.

Adamou, A. T. I., Gridin, D. & Craster, R. V. 2005 Acoustic quasi-modes in slowly varying cylindrical tubes. *Q. J. Mech. Appl. Maths* **58**, 419–438.

Anderson, E., Bai, Z., Bischof, C., Blackford, S., Demmel, J., Dongarra, J., Du Croz, J., Greenbaum, A., Hammarling, S., McKenney, A. & Sorensen, D. 1999 *LAPACK Users' Guide*. Society for Industrial and Applied Mathematics.

Atassi, H. M., Fang, J. & Patrick, S. 1993 Direct calculation of sound radiated from bodies in nonuniform flow. *Trans. ASME: J. Fluids Engng* **115**, 573–579.

Babic, V. M. & Buldyrev, V. S. 1991 *Short-Wavelength Diffraction Theory*. Springer.

Blokhintzev, D. 1946 The propagation of sound in an inhomogeneous and moving medium I. *J. Acoust. Soc. Am.* **18**, 322–328.

Boyd, J. P. 2001 *Chebyshev and Fourier Spectral Methods*, 2nd edn. Dover.

Brambley, E. J. & Peake, N. 2006 Classification of aeroacoustically relevant surface modes in cylindrical lined ducts. *Wave Motion* **43**, 301–310.

Cooper, A. J. & Peake, N. 2000 Trapped acoustic modes in aeroengine intakes with swirling flow. *J. Fluid Mech.* **419**, 151–175.

Cooper, A. J. & Peake, N. 2001 Propagation of unsteady disturbances in a slowly varying duct with mean swirling flow. *J. Fluid Mech.* **445**, 207–234.

Felix, S. & Pagneux, V. 2001 Sound propagation in rigid bends: A multimodal approach. *J. Acoust. Soc. Am.* **110**, 1329–1337.

Felix, S. & Pagneux, V. 2002 Mulitmodal analysis of acoustic propagation in three-dimensional bends. *Wave Motion* **36**, 157–168.

Felix, S. & Pagneux, V. 2004 Sound attenuation in lined bends. *J. Acoust. Soc. Am.* **116**, 1921–1931.

Germano, M. 1982 On the effect of torsion on a helical pipe flow. *J. Fluid Mech.* **125**, 1–8.

Goldstein, M. E. 1978 Unsteady vortical and entropic distortions of potential flows round arbitrary obstacles. *J. Fluid Mech.* **89**, 433–468.

Gridin, D. & Craster, R. V. 2003 Quasi-modes of a weakly curved waveguide. *Proc. R. Soc. Lond.* A **459**, 2909–2931.

Hinch, E. J. 1991 *Perurbation Methods*. Cambridge.

Keefe, D. H. & Benade, A. H. 1983 Wave propagation in strongly curved ducts. *J. Acoust. Soc. Am.* **74**, 320–332.

Keller, J. B. & Rubinow, S. I. 1960 Asymptotic solution of eigenvalue problems. *Ann. Phys.* **9**, 24–75.

Khorrami, M. R., Malik, M. R. & Ash, R. L. 1989 Application of spectral collocation techniques to the stability of swirling flows. *J. Comput. Phys.* **81**, 206–229.

Menzies, R. D. D. 2002 Investigation of S-shaped intake aerodynamics using computational fluid dynamics. PhD thesis, University of Glasgow.

Myers, M. K. 1980 On the acoustic boundary condition in the presence of flow. *J. Sound Vib.* **71**, 429–434.

Ovenden, N. C. 2005 A uniformly valid multiple-scales solution for cut-on cut-off transition of sound in flow ducts. *J. Sound Vib.* **286**, 403–416.

Pagneux, V., Amir, N. & Kergomard, J. 1996*a* A study of wave propagation in varying cross-section waveguides by modal decomposition. Part I. Theory and validation. *J. Acoust. Soc. Am.* **100**, 2034–2048.

Pagneux, V., Amir, N. & Kergomard, J. 1996*b* A study of wave propagation in varying cross-section waveguides by modal decomposition. Part II. Results. *J. Acoust. Soc. Am.* **101**, 2504–2517.

Rienstra, S. W. 1999 Sound transmission in slowly varying circular and annular lined ducts with flow. *J. Fluid Mech.* **380**, 279–296.

Rienstra, S. W. 2003*a* A classification of duct modes based on surface waves. *Wave Motion* **37**, 119–135.

Rienstra, S. W. 2003*b* Sound propagation in slowly varying lined flow ducts of arbitrary cross-section. *J. Fluid Mech.* **495**, 157–173.

Rienstra, S. W. & Eversman, W. 2001 A numerical comparison between the multiple-scales and finite-element solution for sound propagation in lined flow ducts. *J. Fluid Mech.* **437**, 367–384.

Ting, L. & Miksis, M. J. 1983 Wave propagation through a slender curved tube. *J. Acoust. Soc. Am.* **74**, 631–639.